第 30 卷第 10 期
2014 年 10 月

无 机 化 学 学 报
CHINESE JOURNAL OF INORGANIC CHEMISTRY

Vol.30 No.10
2408-2418

二氧化钛多孔纳米片在染料敏化太阳电池中的应用

胡嘉清[1] 雷炳新[1] 孙振范*,[1] 孙 伟[1] 张宪玺*,[2]

([1]海南师范大学化学与化工学院,海口 571158)

([2]聊城大学化学化工学院,山东省化学储能与新型电池技术重点实验室,聊城 252000)

摘要: 运用连续吸附反应法和化学腐蚀–沉积法,用 ZnO/FTO(氟掺杂氧化锡)多孔纳米片为模板,制备了 TiO_2/FTO 多孔纳米片。研究了吸附次数对形貌、光散射性能和染料敏化太阳电池性能的影响。最佳吸附次数为 30,由此得到的太阳能电池的效率、短路电流密度 J_{sc}、开路电压 V_{oc} 和填充因子 *FF* 分别为:5.57%、9.26 mA·cm^{-2}、0.835 V 和 72.04%。这个效率略高于 P25(5.32%),但远高于 ZnO(2.41%)。

关键词: 纳米片; 多孔电极; 二氧化钛; 染料敏化太阳电池

中图分类号: 0614.41$^+$1;TM914.4$^+$2 **文献标识码**:A **文章编号**: 1001-4861(2014)10-2408-11

DOI: 10.11862/CJIC.2014.305

Porous TiO_2 Nanosheets Films for Dye-Sensitized Solar Cells

HU Jia-Qing[1] LEI Bing-Xin[1] SUN Zhen-Fan*,[1] SUN Wei[1] ZHANG Xian-Xi*,[2]

([1]*School of Chemistry and Chemical Engineering, Hainan Normal University, Haikou* 571158, *China*)

([2]*Shandong Provincial Key Laboratory of Chemical Energy Storage and Novel Cell Technology, School of Chemistry and Chemical Engineering, Liaocheng University, Liaocheng, Shandong* 252059, *China*)

Abstract: A strategy was presented for synthesizing TiO_2 nanosheets on fluorine-doped tin oxide (FTO) glass substrate through layer-by-layer absorption and reaction (LBL-AR) method using porous ZnO nanosheets as a template, followed by wet-chemical etching and depositing process. The effect of immersing cycles on the morphology, optical property and performance of dye-sensitized solar cells (DSSCs) has been demonstrated. A maximum efficiency of 5.57% is obtained from 30 cycles of immersing, with a short-circuit current density (J_{sc}) of 9.26 mA·cm^{-2}, open-circuit voltage (V_{oc}) of 0.835 V and fill factor (*FF*) of 72.04%. The maximum efficiency achieved is a little higher than that of cell-P25 (5.32%) and much higher than that of ZnO nanosheets (2.41%).

Key words: nanosheet; porous electrode; TiO_2; dye-sensitized solar cell

As an exceptionally important versatile semiconductor and metal oxide, titanium oxide (TiO_2) has been widely investigated and utilized due to its potential applications in photocatalysis [1], hydrogen production [2], lithium ion batteries [3], sensors [4], dye-sensitized solar cells (DSSCs)[5], and so on. Since the first application of transparent TiO_2 nanocrystalline films to DSSC reported by ORegan and Grtzel in 1991[5], a number of investigations have been carried out to improve the performance of DSSC. A typical DSSC based on the random three-dimensional (3D) networks of mesoporous TiO_2 nanoparticles films has

收稿日期:2014-01-28。收修改稿日期:2014-05-05。

国家自然科学基金(No.21171084),国家重点基础研究发展计划(No.2011CBA00701),海南省应用技术研究与开发(No.ZDXM2014098)和海南省自然科学基金(No.214022 和 213015)资助项目。

*通讯联系人。E-mail:sun@hainnu.edu.cn; zhangxianxi@lcu.edu.cn; Tel: +86-898-31381637

achieved conversion efficiency of more than 12% [6]. The overall performance is still lower than theoretical value due to severe photo-generated electron recombination and poor utilization of near infrared photons. Thus, many research efforts have recently been devoted to develop highly ordered TiO_2 nanoarrays to construct DSSC, such as one-dimensional (1D) nanostructures which can provide direct electrical pathways, such as nanotubes [7-10], nanowires[11-13], nanorods[14-15] and two-dimensional (2D) nanosheets [16]. Highly ordered TiO_2 nanoarrays can increase electron collection and decrease photo-generated electron recombination. Besides, the nanoarrays structures can provide efficient electrolyte diffusion.

Many efforts have already been made to assemble well-organized and oriented TiO_2 nanoarrays on fluorine-doped tin oxide glass (FTO) [10,17-18]. In synthesizing process, many techniques have been applied to construct oriented TiO_2 nanowires or nanotubes arrays, such as template-assisted strategy [19-22], high temperature chemical vapour deposition[23], hydrothermal method[10,24], and anodic oxidation[17-18].

Compared to other template synthesis method, ZnO template is not only a simple synthesizing process and suitable for large area preparation, but also selectively removed. As a low-cost and environmentally friendly approach, ZnO nanorod arrays template-assisted strategy could be utilized to fabricate TiO_2 nanotube arrays with a good alignment and uniformity. Qiu et al.[25] fabricated 1.5 μm thick TiO_2 nanotube arrays on glass substrates using a TiO_2 sol-gel process on ZnO nanorods. Xu et al. [19-20] presented a process for synthesizing vertically aligned TiO_2 nanotube arrays on indium doped tin oxide (ITO) glass substrates through a liquid-phase conversion process using ZnO nanowire arrays as the template. The resulting TiO_2 nanotube arrays with a tube length of 11 and 20 μm yielded power conversion efficiencies up to 3.6% and 6.1%, respectively. Zhuge et al.[21] introduced a facile route to prepare aligned TiO_2 nanotube arrays involving layer-by-layer adsorption and reaction (LBL-AR) methods using ZnO nanowire arrays as the template. The preliminarily optimized conversion efficiency of 5.7% was obtained with a 20 μm hierarchical nanotube array as the photoanode[21]. Recently, Yuan et al.[26] reported anatase TiO_2 nanosheets on Si substrate by a liquid-phase deposition method using 2D ZnO nanosheet arrays as the template. However, to the best of our knowledge, there have been few studies on the growth of 2D TiO_2 nanosheet films on FTO glass.

Here, we report the preparation of porous TiO_2 nanosheets films on the FTO glass using porous ZnO nanosheets as the template by applying the layer-by-layer absorption and reaction (LBL-AR) method, followed by wet-chemical etching and depositing process. The effect of immersing cycles on dye absorbed, the morphologies, and the electron transport property is also studied.

1 Experimental

1.1 Preparation of the TiO_2 blocking layer

The FTO glasses were well cleaned in acetone, ethanol, and deionized (DI) water each for 15 min ultrasonically. Finally, they were dried in air at 60 ℃. TiO_2 blocking layer was deposited on FTO glass by spin-coating TiO_2 collosol solution [27-28]. The TiO_2 blocking layer on FTO glass was calcined at 550 ℃ for 1 h using a heating rate of 2 ℃·min^{-1}.

1.2 Preparation of oriented ZnO nanosheets films

Based on the reported procedure[29], the oriented ZnO porous nanosheets can be facilely prepared in large scale via a hydrothermal method. In a typical synthesis, 16 mmol of zinc nitrate hexahydrate ($Zn(NO_3)_2 \cdot 6H_2O$) and 48 mmol urea ($(NH_2)_2CO$) were dissolved in 40 mL of deionized water under constant stirring. The TiO_2 coated FTO glass was placed at an angle against the wall of the Teflon-liner with the conducting side facing down. The hydrothermal synthesis was conducted at 120 ℃ for 3 h in an electric oven. After synthesis, the autoclave was naturally cooled to room temperature. The as-grown films were thoroughly rinsed with deionized water, and then dried in an electronic oven at 70 ℃. Finally, the films were calcined at 500 ℃ for 30 min at a heating

rate of 2 ℃·min^{-1}.

1.3 Fabrication of TiO_2 nanosheets films

The as-calcined ZnO nanosheets films were successively immersed in transparent TiO_2 sol, ethanol, deionized water, ethanol for each 30 s, and this process comprised one LBL-AR cycle. The TiO_2 sol was composed of 0.5 mol·L^{-1} tetrabutyl titanate (TBT) and 0.5 mol·L^{-1} acetylacetone (acac) in absolute ethanol. The ZnO/TiO_2 nanosheets samples were calcined at 300 ℃ for 1 h to remove the organic residues, followed by mild etching in dilute $TiCl_4$ (40 mmol·L^{-1}) for 10 h at room temperature to remove ZnO thoroughly and simultaneously deposit TiO_2 for the formation of TiO_2 nanosheets.

1.4 Morphology and structural characterization

The phase purity of the products was characterized by X-ray diffraction (XRD) on a Bruker D8 Advance X-ray diffractometer. The beam was collimated, compressed and frequency filtered by a Gbel mirror and V-Groove (Cu $K\alpha 1$ radiation, λ = 0.154 06 nm), employing a scanning rate of 10°·min^{-1}, in the 2θ range from 20° to 80°. The field emission scanning electron microscopy (FE-SEM, JEOL, JSM-7100F) was performed to characterize the morphology and size using excitation voltage of 15 kV. The transmission electron microscopy (TEM, JEOL, JEM-2010-HR, 200 kV), high-resolution transmission electron microscopy (HRTEM) and selected area electron diffraction (SAED) patterns were performed on a JEOL-2010-HR transmission electron microscopy. UV-Vis diffuse reflectance spectra and absorption spectra were recorded on a UV-Vis-NIR spectrophotometer (UV-1901, Beijing Purkinje General Instrument Co. Ltd., China) to analyse the diffuse reflectance of films and dye amounts detached from films, respectively.

1.5 Fabrication and photovoltaic measurement of DSSCs

P25 powder (1.0 g) was ground for 40 min in the mixture of ethanol (8.0 mL), acetic acid (0.2 mL), terpineol (3.0 g) and ethyl cellulose (0.5 g) to form a slurry, and then the slurry was sonicated for 5 min in an ultrasonic bath, finally to form a viscous white TiO_2 paste. The P25 electrodes were prepared via screen-printing of the above P25 paste on the FTO substrate. P25 films were heated under an air flow at 500 °C for 30 min. Both the as-prepared porous TiO_2 nanosheets and P25 electrodes were immersed in 40 mmol·L^{-1} $TiCl_4$ solution at 70 ℃ for 30 min, then calcined at 520 ℃ for 30 min. After cooling down to ~80 ℃, the electrodes were immersed into 0.5 mmol·L^{-1} N719 dye ($[(C_4H_9)_4N]_2[Ru(Ⅱ)L_2(NCS)_2]$, where L=2,2′-bipyridyl-4, 4′-dicarboxylic acid, Solaronix SA, Switzerland) in acetonitrile/tert-butanol (1∶1, *V*/*V*) for 16 h at room temperature. Afterwards, these films were rinsed with acetonitrile in order to remove physisorbed N719 dye molecules. To evaluate their photovoltaic performance, the dye-sensitized TiO_2/FTO glass films were sandwiched together with Pt coated FTO glass which was used as the counter electrode. Platinized counter electrodes were fabricated by thermal-deposition of H_2PtCl_6 solution (5 mmol·L^{-1} in isopropanol) onto FTO glass. The electrolyte, 0.03 mol·L^{-1} I_2, 0.05 mol·L^{-1} LiI, 0.6 mol·L^{-1} 1-methyl-3-propylimidazolium iodide (PMII), 0.10 mol·L^{-1} guanidinium thiocyanate, and 0.5 mol·L^{-1} tert-butylpyridine in acetonitrile and valeronitrile (85∶15, *V*/*V*), was introduced from a hole made on the counter electrode into the space between the sandwiched cells.

The current-voltage characteristics of DSSCs were recorded using a Keithley model 2400 digital source meter under one sun illumination (AM 1.5G, 100 mW·cm^{-2}) with a solar light simulator (Oriel, Model: 94041A). A 450 W Xenon lamp was served as a light source and its incident light intensity was calibrated with a NREL-calibrated Si solar cell to one sun illumination light intensity before each measurement. The active area of photoanode was 0.16 cm^2. The electrochemical impedance spectroscopy (EIS) measurements were performed with a Zennium electrochemical workstation (ZAHNER) with the frequency range from 10 mHz to 1 000 kHz. The magnitude of the alternative signal was 10 mV. The impedance measurements were carried out under forward bias of −0.85 V in the dark. Intensity-modulated photocurrent spectroscopy (IMPS)

measurement was carried out on a electrochemical workstation (Zahner, Zennium) with a frequency response analyzer under a modulated green light emitting diodes (505 nm) driven by a source supply (Zahner, PP211), which can provide both dc and ac components of the illumination. The modulated light intensity was 10% or less than the base light intensity. The frequency range was set from 1 000 kHz to 0.1 Hz.

2 Results and discussion

2.1 XRD analysis

Fig.1 shows XRD patterns of ZnO nanosheets, TiO_2 coated ZnO nanosheets (ZnO/TiO_2) and the as-prepared TiO_2 nanosheets on the FTO glass. As can be seen from Fig.1a, the XRD pattern of ZnO nanosheets can be assigned to hexagonal wurtzite structure of ZnO (PDF No. 36-1451). The XRD pattern of ZnO/TiO_2 (Fig.1b) shows the characteristic diffraction peaks of ZnO, while the characteristic diffraction peaks of TiO_2 does not obviously appear, which may be due to the formation of amorphous TiO_2. The XRD pattern shown in Fig.1c reveals that the diffraction peaks of the as-prepared porous TiO_2 nanosheets on FTO glass (30 cycles) are consistent with the anatase phase (PDF No.21-1272), but there

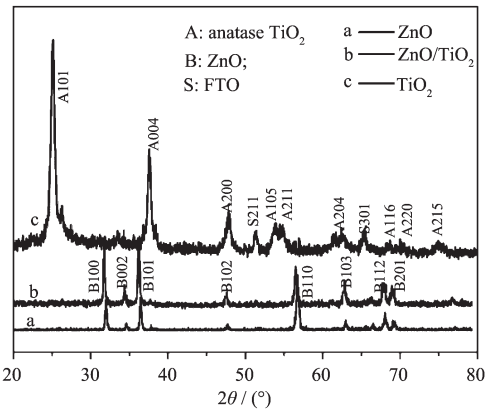

Fig.1 XRD patterns of ZnO nanosheets, TiO_2 coated ZnO nanosheets (ZnO/TiO_2) and the as-prepared TiO_2 nanosheets on FTO glass

are several small peaks in the pattern, corresponding to the SnO_2 phase (FTO glass)[30]. No crystalline ZnO is detected. The result indicates that dilute $TiCl_4$ solution removes ZnO thoroughly.

2.2 FE-SEM analysis

A previous literature report[31] demonstrated that it was possible to transform ZnO porous nanosheets to TiO_2 porous nanosheets by directly treating ZnO porous nanosheets in an aqueous solution of $TiCl_4$. However, the overall morphology and porous nanosheet structure were destroyed. Fig.2 shows the as-calcined ZnO nanosheets films that are directly

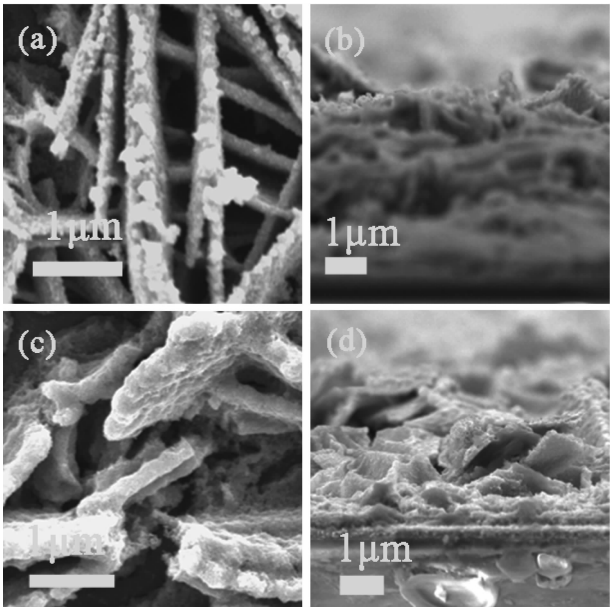

Fig.2 FE-SEM images of TiO_2 coated ZnO nanosheets obtained by directly immersing porous ZnO nanosheets in 40 mmol·L^{-1} $TiCl_4$ aqueous solution for 1 h (a, b) and 2 h (c, d), respectively

immersed in 40 mmol·L^{-1} $TiCl_4$ aqueous solution for 1~2 h. Fig.2a, b exhibit TiO_2 coated ZnO nanosheets can inherit the geometrical shape of the ZnO nanosheet template, but the length of nanosheets decreases to 4.2 μm. When the ZnO nanosheets films are immersed in $TiCl_4$ for 2 h, the geometrical shape of nanosheets is destroyed, and the length of nanosheets decreases to 2.3 μm (Fig.2c, d). Herein, it is necessary to improve this process by depositing a thin TiO_2 polycrystalline shell on ZnO nanosheets. To obtain porous TiO_2 nanosheets with a high-quality structure, the simple LBL-AR method is used to deposit a thin TiO_2 shell on ZnO porous nanosheets. The TiO_2 shell serves as the skeleton to maintain the overall morphology, and porous nanosheet structure and the polycrystalline nature ensure the penetration of $TiCl_4$ solution through the TiO_2 shell. The specific process is illustrated as follows. The LBL-AR method involves successively immersing porous ZnO nanosheets into transparent TiO_2 sol, ethanol, water, and back into ethanol, followed by sintering at 300 ℃ for 1 h. The transparent TiO_2 sol modified with acetylacetone can avoid unfavorable homogenous precipitations during the hydrolysis reaction. TiO_2 coated ZnO nanosheets are treated in $TiCl_4$ solution at room temperature for 10 h. During this process, the cation exchange reaction between Zn^{2+} and Ti^{4+} occurs, which could be qualitatively understood in terms of hard-soft acid-base theory[31-32]. Because Ti^{4+} is a harder acid than Zn^{2+}, Ti^{4+} could bind strongly with O^{2-} to form TiO_2. The conversion of ZnO to TiO_2 material is strongly favored because of a thermodynamic driving force of about −249 kJ·mol^{-1} [31-32]. After the treating process, TiO_2 porous nanosheets with hollow structures are formed. The formation of a hollow structure is attributed to cation exchange accompanied by the nanoscale Kirkendall effect. That is, Ti^{4+} diffusion is limited and the core species (Zn^{2+}) diffuse outwards, generating a void space inside the cores of the particles[31,33].

Zhuge et al.[21] found that ZnO template could be selectively removed, but this process suffers from the poor adhesion between TiO_2 nanotube and FTO glass substrate. After spin-coating TiO_2 sol to replace ZnO seed layer, the TiO_2 blocking layer with 200 nm in thickness is formed on the FTO glass substrates, which not only reduces charge recombination as the blocking layer, but also protects the as-prepared TiO_2 nanosheets films from detaching the FTO glass in the wet-chemical etching and depositing process. Fig.3a~c represent FE-SEM images of the as-calcined ZnO nanosheets films on TiO_2 coated FTO glass substrates. It can be seen that the ZnO films are composed of porous nanosheets with a thickness ca. 80 nm, in agreement with the results of Ref [29]. In addition, ZnO nanosheets have a good uniformity in a large scale without any crack gaps. Fig.3b shows the ZnO nanosheets with a thickness of ca. 18.7 μm. Moreover, these ZnO nanosheets are perpendicular to FTO substrate. As for the higher magnification cross-sectional FE-SEM image shown in Fig.3c, ZnO nanosheets are porous, and some pores are connected with each other. The formation of pores may be attributed to the release of H_2O and CO_2 derived from decomposition of urea during the heat treatment [29].

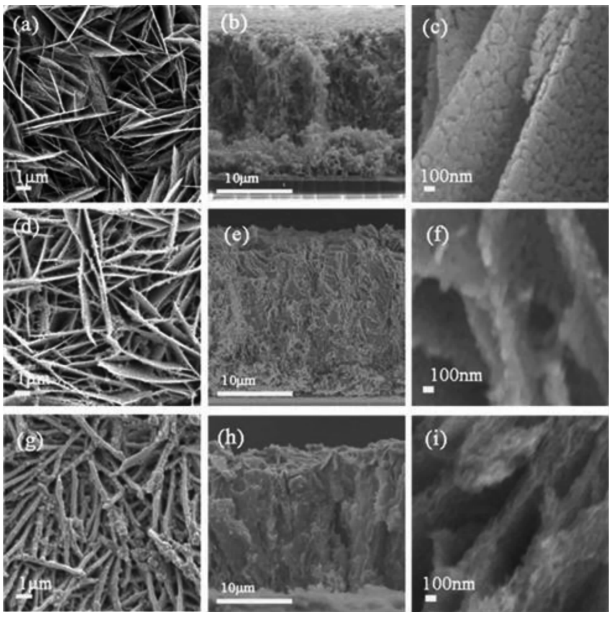

Fig.3 FE-SEM images of the as-calcined ZnO nanosheets grown on the TiO_2 blocking layer FTO glass substrates (a~c); FE-SEM images of TiO_2 coated ZnO nanosheets abtained after LBL-AR method (d~f); FE-SEM images of porous TiO_2 nanosheets after wet-chemical etching and depositing process (g~i)

Fig.3d ~f show FE-SEM images of TiO_2 coated ZnO nanosheets obtained after LBL-AR method (30 cycles). Compared to bare ZnO nanosheets (Fig.3a~c), it can be seen that the thickness of TiO_2 coated ZnO nanosheets becomes thicker after LBL-AR method. When the LBL-AR cycle is 30, the thickness of TiO_2 coated ZnO nanosheets is 89 nm. After 30 LBL-AR cycles, large numbers of tiny TiO_2 nanocrystalline are modified on both surfaces of the primary ZnO nanosheets uniformly, as displayed in Fig.3d. In addition, the framework with the porous morphology still exists, as shown in Fig.3d and 3e. It is clear from the image of Fig.3d that there is evidence for the presence of TiO_2 nanoparticles. The concrete TiO_2 nanoparticles are derived from tetrabutyl titanate hydrolysis into TiO_2 by immersing into distilled water. The obtained TiO_2 coated ZnO nanosheets is calcined at 300 ℃, followed by mild etching in $TiCl_4$ (40 $mmol \cdot L^{-1}$) solution at room temperature to remove the inner core of ZnO and simultaneously deposit TiO_2 for forming porous TiO_2 nanosheets. Fig.3g ~i show FE-SEM images of porous TiO_2 nanosheets (30 cycles) after wet-chemical etching and depositing process. It can be found that TiO_2 nanosheets faithfully inherit the shape of the porous ZnO nanosheets. TiO_2 nanosheets remain 18.7 μm long, but the thickness of nanosheets increases to 133 nm because TiO_2 deposits on both the surfaces of nanosheets.

Fig.4 shows the top and cross-sectional FE-SEM images of the as-calcined TiO_2 nanosheet with different immersing cycles. After wet-chemical etching and depositing process, the samples are uniformly decorated with TiO_2 nanoparticles. As shown in the images of Fig.4c, 4f, 4i, 4l, TiO_2 films inherit the original shape of the porous ZnO nanosheets. There is no evidence of lodgings, cracks or overlayers in the FE-SEM images (Fig.4a, 4d, 4g and 4j). The thicknesses of TiO_2 nanosheets films remain unchanged after the wet-chemical etching and depositing process. However, the distance between the neighbour nanosheets gets shorter. The thickness of TiO_2 nanosheets increases from 107 nm, 115 nm, 126 nm to 142 nm with the increase of LBL-AR cycle number from 20, 25, 30 to 35, respectively.

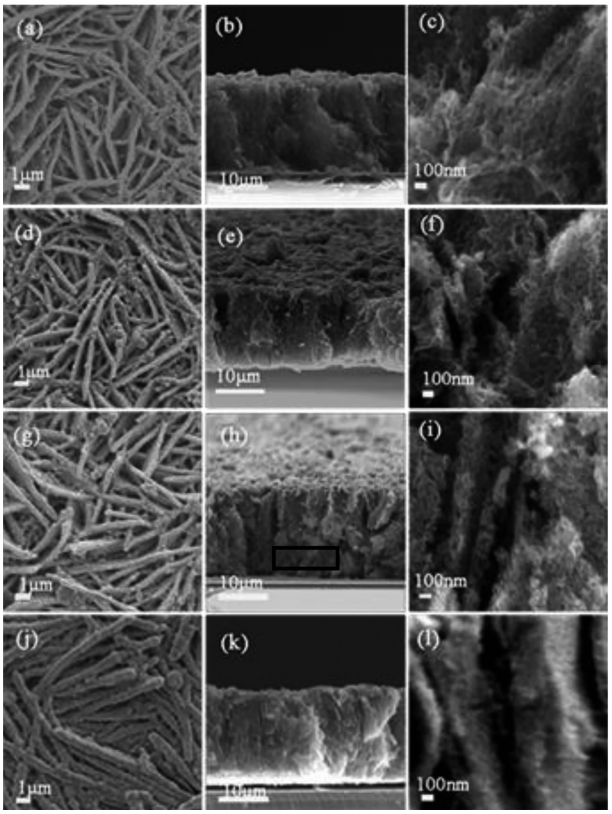

Fig.4　FE-SEM images of the as-calcained TiO_2 nanosheets with various immersing cycles. (a) top views, (b) cross-sectional views and (c) the enlarged views images of immersing 20 cycles; (d~f), (g~i), (i~l), corresponding to 25, 30, 35 cycles images, respectively

The energy dispersive X-ray (EDX) spectrum of Fig.5, taken from the part marked in Fig.4h, shows only the presence of the Ti and O related peaks without any Zn related peaks, further confirming that dilute $TiCl_4$ solution removes ZnO completely.

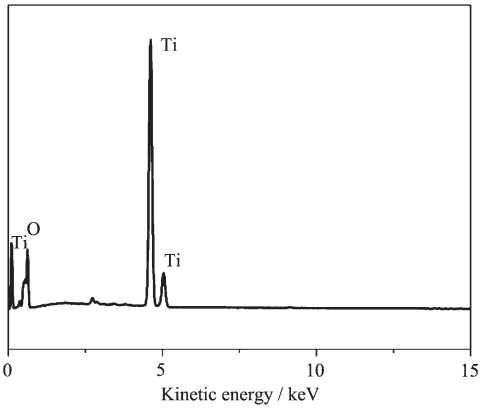

Fig.5　EDX spectra for the marked area in Fig.4h

2.3 TEM analysis

Fig.6a shows the TEM image of a single TiO_2 nanosheet obtained by scratching from FTO glass. From this TEM image, it is estimated that the nanosheet is composed of nanoparticle with a diameter of 10~20 nm. It can also be seen that the single sheet has lots of pores. The selected-area electron diffraction (SAED) pattern (inset of Fig.6a) reveals the polycrystalline anatase composition of TiO_2 nanosheets. In addition, the HRTEM image of a single TiO_2 nanosheet (Fig.6b) exhibits clear and coherent lattice fringes running through the whole nanosheet. The HRTEM image indicates a lattice spacing of 0.35 nm, which can be ascribed to the (101) planar spacing of the TiO_2 nanosheet.

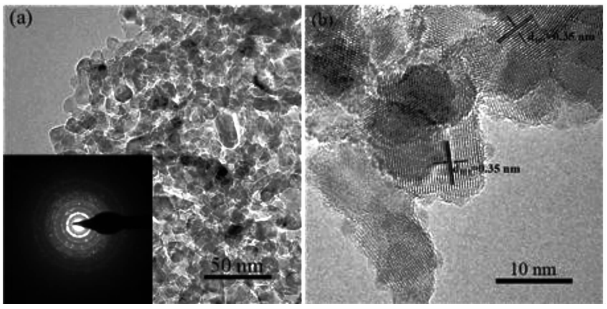

Fig.6 TEM (a) and HRTEM (b) images of the as-calcined TiO_2 nanosheets with 30 cycles. The polycrystalline nature is reflected by the inset selective area electron diffraction (SAED)

2.4 Photovoltaic performance test

The effect of immersing cycles on the performance of porous TiO_2 nanosheets electrode is measured and analyzed. The performances of DSSCs based on these nanoporous photoanode are measured under simulated sunlight. Fig.7 shows the current-voltage (*J-V*) curves of the four DSSCs, and the corresponding photovoltaic parameters are summarized in Table 1. As can be seen from the Table 1, the J_{sc} increases from 6.95 mA·cm^{-2} to 7.72 mA·cm^{-2}, 9.26 mA·cm^{-2} and then decreases to 8.37 mA·cm^{-2} with the immersing cycles from 20, 25, 30 to 35, leading to the change of power conversion efficiency from 4.29%, to 4.79%, 5.57% and 5.02%. Cell-4 (35 cycles) shows worse performance than that of cell-3 (30 cycles), which can be due to larger recombination rate of cell-4. It is worth noting that the most efficient photovoltaic performance of 5.57% is obtained from 30 LBL-AR cycles. The initial increase of the J_{sc} can be attributed to the larger amount of dye and the scattering effect (shown in Table 1 and Fig.8). However, with further increase of cycle number, for example, from 30 to 35, the J_{sc} reduces from 9.26 mA·cm^{-2} to 8.37 mA·cm^{-2}, resulting in a decrease of DSSC efficiency from 5.57% to 5.02%. The decrease of the J_{sc} for 35 cycles (cell-4) can be attributed to the larger amount of surface defects and recombination centers. The photovoltage declines gradually from 865 mV (cell-1, 20 cycles) to 828 mV (cell-4, 35 cycles) along with the increasing cycle number due to the

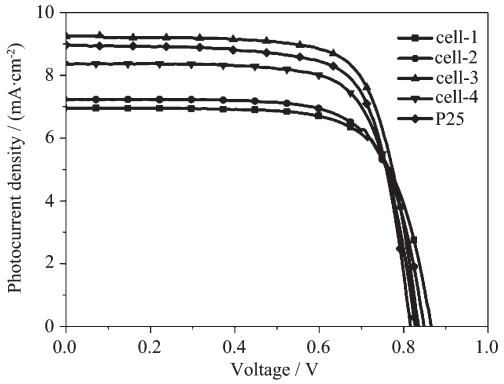

Fig.7 *J-V* charactercteristics of TiO_2 nanosheets based DSSCs with various immersing cycles and commercial P25 nanoparticles film under AM 1.5G illumination (100 mW·cm^{-2}) (20 cycles: cell-1, 25 cycles: cell-2, 30 cycles: cell-3, 35 cycles: cell-4)

Table 1 Characteristics and photovoltaic parameters of the samples

Samples	V_{oc} / V	J_{sc} / (mA·cm^{-2})	*FF* / %	η / %	Adsorbed dye / (μmol·cm^{-2})
Cell-1	0.865	6.95	71.36	4.29	0.129 9
Cell-2	0.862	7.72	71.53	4.79	0.150 0
Cell-3	0.835	9.26	72.04	5.57	0.162 1
Cell-4	0.828	8.37	72.43	5.02	0.180 8
P25	0.816	8.90	73.20	5.32	0.208 9

increase in the thickness of TiO_2 nanosheets, which provides additional charge recombination sites resulting in larger recombination rate (see the following discussion of EIS).

For comparison with cell-3, P25 electrode with the thickness of ca.18.7 μm is used as photoanode for DSSC applications (shown in Table 1 and Fig.7). Consequently, the J_{sc} and V_{oc} for P25 based DSSCs are 8.90 mA·cm^{-2} and 816 mV, respectively, which are inferior to that of cell-3 (9.26 mA·cm^{-2} and 835 mV), leading to an enhancement in efficiency for the latter (5.57%), somewhat better than its P25 nanoparticles counterpart (5.32%). The enhanced efficiency for the porous TiO_2 nanosheets could be ascribed to the superior light scattering ability for enhanced light-harvesting efficiency, efficient charge collection, electrolyte penetration as well as suppressed charge recombination due to the 2D direct electric transfer pathway with less grain boundaries and defects[16,26].

The photocurrent is strongly related to amounts of dye and the scattering ability of the TiO_2 photoelectrode. The amounts of dyes adsorbed on the samples are obtained by measuring the UV-Vis absorption spectra of solutions containing dyes detached from the films in 0.1 mol·L^{-1} NaOH (3 mL). With increasing the immersing cycle number, it is found that the dye amount increases from the increased surface area of the TiO_2 nanosheets, as shown in Table 1. The increase in the number of adsorbed dye molecules will lead to more photo-generated electrons and higher photocurrents. Although more dye amounts for cell-4, the J_{sc} experiences a slight decrease from 9.26 mA·cm^{-2} to 8.37 mA·cm^{-2}, which can be attributed to a larger amount of surface defects and recombination centers. This is in good agreement with the *J-V* data.

On the other hand, higher light scattering ability is another way to improve the light harvesting efficiency. In order to investigate the light scattering ability of the four films, the UV-Vis reflectance spectra are further characterized and shown in Fig.8. The intensity of reflectance spectrum of the films gradually increases with increasing LBL-AR cycle

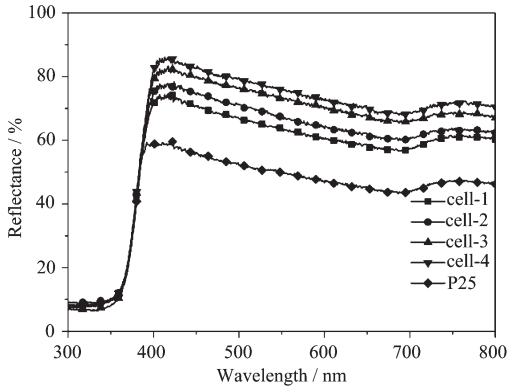

Fig.8 Reflectance spectra of as-calcined TiO_2 nanosheets films of various immersing cycles and commercial P25 nanoparticles photoanode (20 cycles: cell-1, 25 cycles: cell-2, 30 cycles: cell-3, 35 cycles: cell-4)

numbers, which is ascribed to the increase of the thickness of nanosheets from 107 nm to 142 nm. However, the increase of the thickness is corresponding to the amount of surface defects and recombination centers. Hence, both the higher dye loading and superior light scattering ability are contributed to the higher light harvesting efficiency to enhance the short-circuit current density and power conversion efficiency.

Generally, three characteristics semicircles can be obtained from electrochemical impedance spectra (EIS) in the frequency range between 10^6 Hz and 10^{-2} Hz. The high-frequency semicircle corresponds to the charge-transfer resistance at the interface of the counter electrode and the electrolyte (R_{ct1}). The middle-frequency semicircle is related to electron transfer and recombination at the TiO_2/dye/electrolyte interfaces (R_{ct2}). The low-frequency semicircle corresponds to Nernst diffusion of I^-/I_3^- within the electrolyte (Z_w)[34-37]. Fig.9 shows the impedance spectra of different photoanodes and the fitted data are summarized in Table 2. As shown in Fig.9, two main semicircles are observed and the third semicircle of Z_w is not obvious and overlapped by R_{ct2}, which is due to the low viscosity of the present electrolyte[38-40]. The values of R_s and R_{ct1} of the four cells are similar, because the same electrolyte and counter electrode are used which lead to similar fill factors. However, the R_{ct2} value of cell-1, cell-2, cell-3, cell-4 and cell-

Table 2 Series resistance (R_s), charge transfer resistance (R_{ct1}), and electron transfer and recombination (R_{ct2}) of the DSSCs fabricated using different photoanodes

Cell	R_s / Ω	R_{ct1} / Ω	R_{ct2} / Ω	τ / ms
Cell-1	22.36	10.22	190.4	95.4
Cell-2	22.31	10.18	143.7	79.2
Cell-3	22.27	10.15	112.4	66.5
Cell-4	22.29	10.12	85.5	42.7
P25	22.24	10.09	66.9	39.3

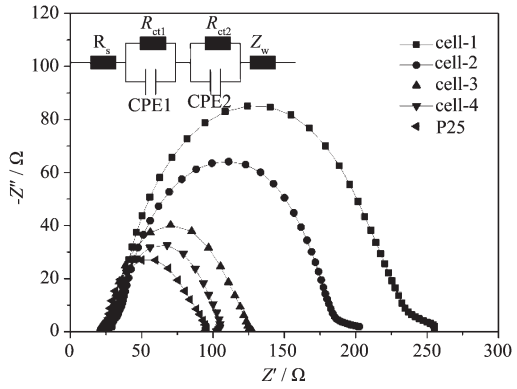

Fig.9 Nyquist plot of four representative DSSCs fabricated with different immersing cycles and commercial P25 nanoparticles film. (20 cycles: cell-1, 25 cycles: cell-2, 30 cycles: cell-3, 35 cycles: cell-4). The equivalent circuit model used to extract the impedance parameters is shown in the inset

P25 is 190.4, 143.7, 112.4, 85.5 and 66.9 Ω, respectively. Both the slower electron recombination process and the higher dye loading result in a larger R_{ct2}[41]. The electron lifetime by *Z*-view with expression: τ =CPE-T ×R, where τ represents the lifetime and CPE-T represents the chemical capacitance. The τ value of cell-1, cell-2, cell-3, cell-4 and cell-P25 is 95.4, 79.2, 66.5, 42.7 and 39.3 ms, respectively. The higher τ implies higher V_{oc}. This result is in concurrence with the significant reduction of V_{oc} displayed in the *J-V* results.

The electron transport time (τ_d) can be calculated from the expression $\tau_d = 1/(2\pi f_d)$, where f_d is the characteristic frequency of the minimum intensity-modulated photocurrent spectroscopy (IMPS) imaginary component. Fig.10 shows the electron transport time (τ_d) of the two DSSCs (cell-3 and cell-P25) as a function of the incident light intensity, which is derived from IMPS. Clearly, the electron transport time corresponding to the 2D TiO_2 nanosheets is shorter than that for P25 (Fig.10). The results indicate that 2D nanosheets can provide direct pathways for electron transport. Short electron transport time means a fast electron transport rate in the photo-electrode, and a low probability of electron recombination, which is important for improving the charge-collection efficiency and the power conversion efficiency of DSSCs[42].

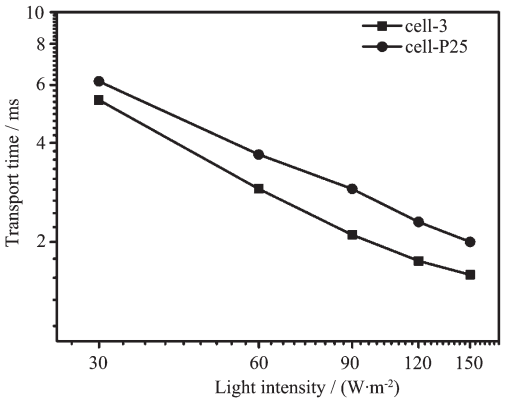

Fig.10 Electron transport time of DSSCs based on TiO_2 nanosheets and P25 photoanodes, measured by IMPS at different light densities

For comparison with cell-3, porous ZnO nanosheets film with a thickness of ca.18.7 μm is also used as photo-anode for DSSC applications. As shown in Fig.11, the power conversion efficiency (2.41%) accompanied by J_{sc} of 5.86 mA·cm^{-2}, V_{oc} of 665 mV, and FF of 61.84% is achieved for the DSSC based on porous ZnO nanosheets film with a thickness of 18.7 μm. As expected, the conversion of ZnO nanosheets to TiO_2 nanosheets results in considerable improvement in J_{sc}, V_{oc} and FF: the J_{sc} increases from 5.86 mA·cm^{-2} to 9.26 mA·cm^{-2}, the V_{oc} from 0.665 V to 0.835 V and FF from 61.84% to 72.04% after ZnO nanosheets are converted to TiO_2 nanosheets. As a result of the

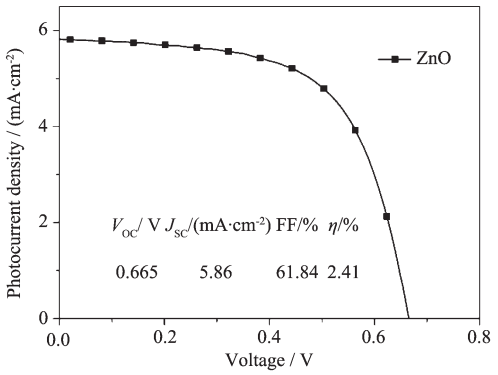

Fig.11　*J-V* charactercteristics of DSSC based on ZnO nanosheets

increased J_{sc}, V_{oc} and FF, the η increases from 2.41% to 5.57% as ZnO is converted to TiO_2.

3　Conclusions

In summary, porous TiO_2 nanosheets films with well-defined morphologies have been prepared using ZnO nanosheets as the templates via LBL-AR method, followed by wet-chemical etching and depositing process. We investigate the effect of cycle in TiO_2 sol on the morphologies and the efficiency of the DSSCs. The maximum efficiency of 5.57% has been obtained at the 30 immersing cycles, which is a little higher than that of cell-P25 (5.32%) and much higher than that of ZnO nanosheets (2.41%). The IMPS result indicates that 2D nanosheets can enhance electron transport rate by providing direct pathways for electron transport.

References:

[1] Linsebigler A L, Lu G Q, Yates J T. *Chem. Rev*., **1995**,**95**(3):735-758

[2] Fujishima A, Honda K. *Nature*, **1972**,**238**(5358):37-38

[3] Han H, Song T, Lee E K, et al. *ACS Nano*, **2012**,**6**(9):8308-8315

[4] Tian W C, Ho Y H, Chen C H, et al. *Sensors*, **2013**,**13**(1):865-874

[5] O′Regan B, Grtzel M. *Nature*, **1991**,**353**:737-740

[6] Yella A, Lee H W, Tsao H N, et al. *Science*, **2011**,**334**(6056):629-634

[7] SUN Lan(孙岚), LI Jing(李静), ZHUANG Hui-Fang(庄慧芳), et al. *Chinese. J. Inorg. Chem*.(无机化学学报), **2007**,**23**(11):1841-1850

[8] GE Zeng-Xian(葛增娴), WEI Ai-Xiang(魏爱香), LIU Jun(刘俊), et al. *Chinese. J. Inorg. Mater.* (无机材料学报), **2010**,**25**(10):1105-1109

[9] Zhu K, Neale N R, Miedaner A, et al. *Nano Lett.*, **2007**,**7**(1):69-74

[10]Lei B X, Liao J Y, Zhang R, et al. *J. Phys. Chem. C*, **2010**,**114**(35):15228-15233

[11]Liu B, Boercker J E, Aydil E S. *Nanotechnology*, **2008**,**19**(50):505604-505609

[12]TANG Yu-Xin(汤育欣), TAO Jie(陶杰), TAO Hai-Jun(陶海军), et al. *Acta Phys.-Chim. Sin.*(物理化学学报), **2008**,**24**(6):1120-1126

[13]Liao J Y, Lei B X, Chen H Y, et al. *Energy Environ. Sci*., **2012**,**5**(2):5750-5757

[14]Liu B, Aydil E S. *J. Am. Chem. Soc*., **2009**,**131**(11):3985-3990

[15]LÙ M Q, Zheng D J, Ye M D, et al. *Nanoscale*, **2012**,**4**(19):5872-5879

[16]Zhu H, Yang J Y, Feng S L, et al. *Appl. Phys. A*, **2011**,**105**(3):769-774

[17]Mor G K, Shankar K, Paulose M, et al. *Nano Lett*., **2006**,**6**(2):215-218

[18]Varghese O K, Paulose M, Grimes C A. *Nat. Nanotechnol*., **2009**,**4**:592-597

[19]Xu C K, Shin P H, Cao L L, et al. *Chem. Mater.*, **2010**,**22**(1):143-148

[20]Xu C K, Gao D. *J. Phys. Chem. C*, **2012**,**116**(12):7236-7241

[21]Zhuge F W, Qiu J J, Li X M, et al. *Adv. Mater.*, **2011**,**23**(11):1330-1334

[22]Qiu J J, Zhuge F W, Lou K, et al. *J. Mater. Chem*., **2011**,**21**(13):5062-5068

[23]Lee J C, Kim T G, Lee W, et al. *Cryst. Growth Des.*, **2009**,**9**(10):4519-4523

[24]Wu W Q, Lei B X, Rao H S, et al. *Sci. Rep*., **2013**,**3**:1352-1358

[25]Qiu J J, Yu W D, Gao X D, et al. *Nanotechnology*, **2006**,**17**(18):4695-4698

[26]Yuan J J, Li H D, Wang Q L, et al. *Mater. Lett.*, **2012**,**81**:123-126

[27]Lei B X, Fang W J, Hou Y F, et al. *J. Photochem. Photobiol. A*: *Chem*., **2010**,**216**(1):8-14

[28]Liao J Y, Lei B X, Kuang D B, et al. *Energy Environ. Sci*., **2011**,**4**(10):4079-4085

[29]Wang X Y, Tian Z P, Yu T, et al. *Nanotechnology*, **2010**,**21**(6):065703-065707

[30]Yu J G, Fan J J, Lü K L. *Nanoscale*, **2010**,**2**(10):2144-2149

[31]Muduli S, Game O, Dhas V, et al. *Energy Environ. Sci.*, **2011**,**4**(8):2835-2839

[32]Chen H N, Zhu L Q, Hou Q, et al. *Chemsuschem*, **2013**,**6**(6):983-988

[33]Park J, Zheng H M, Jun Y W, et al. *J. Am. Chem. Soc*., **2009**,**131**(39):13943-13945

[34]Kim Y J, Lee M H, Kim H J, et al. *Adv. Mater*., **2009**,**21**(36):3668-3673

[35]Zhou Y F, Xiang W C, Chen S, et al. *Electrochim. Acta*, **2009**,**54**(26):6645-6650

[36]Wang Q, Moser J E, Grtzel M. *J. Phys. Chem. B*, **2005**,**109**(31):14945-14953

[37]Phadke S, Pasquier A D, Birnie D P. *J. Phys. Chem. C*, **2011**,**115**(37):18342-18347

[38]Yin X, Xue Z S, Liu B. *J. Power Sources*, **2011**,**196**(4):2422-2426

[39]Lai Y H, Lin C Y, Chen H W, et al. *J. Mater. Chem*., **2010**,**20**(42):9379-9385

[40]Ito S, Ha N L C, Rothenberger G, et al. *Chem. Commun*., **2006**:4004-4006

[41]Hoshikawa T, Yamada M, Kikuchi R, et al. *J. Electrochem. Soc*., **2005**,**152**(2):E68-E73

[42]Qu J, Li G R, Gao X P. *Energy Environ. Sci*., **2010**,**3**(12):2003-2009